Nanoscale

PAPER

View Article Online
View Journal | View Issue

Cite this: *Nanoscale*, 2025, **17**, 5778

Copper nanoclusters with aggregation-induced emission: an effective photodynamic antibacterial agent for treating bacteria-infected wounds†

Zhen Jiang,[a] Yongqi Wei,[a] Yun Wang,[c] Songjie Han,[a] Ze Li,[a] Sihang Liu,[a] Zihao Wang,[a] Zhijun Li,[b] Ting Feng,[a] Haiguang Zhu *[a,b] and Xun Yuan *[a]

Received 11th November 2024,
Accepted 19th January 2025

DOI: 10.1039/d4nr04718d

rsc.li/nanoscale

Designing antibacterial agents with broad-spectrum antibacterial effects and resistance-free properties is essential for treating bacteriainfected wounds. In this study, we present the design of copper nanoclusters (Cu NCs) that exhibit aggregation-induced emission (AIE). This was achieved by controlling the aggregation state of ligand layers (cysteine and chitosan) through the manipulation of pH and temperature. The AIE properties, characterized by strong photoluminescence (PL), a large Stokes shift, and microsecond-long lifetimes, enable these Cu NCs to generate significant amounts of reactive oxygen species (ROS) upon light illumination for efficient bacterial elimination without inducing drug resistance. As a result, they effectively inactivate various microbial pathogens, including Gram-negative and Gram-positive bacteria, as well as *Candida albicans* (*C. albicans*), achieving elimination rates of 99.52% for *Escherichia coli* (*E. coli*), 98.89% for *Staphylococcus aureus* (*S. aureus*), and 94.60% for *C. albicans in vitro*. Furthermore, the natural antibacterial properties of chitosan and Cu species enhance the photodynamic antibacterial efficacy of the AIE-typed Cu NCs. Importantly, *in vivo* experiments demonstrate that these Cu NCs can effectively eradicate bacteria at infection sites, reduce inflammation, and promote collagen synthesis, facilitating nearly 100% wound recovery in *S. aureus*-infected wounds within 9 days. The findings of this study are of considerable significance, providing a foundation for the application of AIE-typed Cu NCs in photodynamic nanotherapy for bacterial infections.

1. Introduction

Highly luminescent metal nanoclusters (NCs) with aggregation-induced emission (AIE) have emerged as a novel class of functional materials, characterized by their ultra-small core size (≤3 nm),[1–3] excellent photoluminescence (PL),[4–6] large Stokes shift (>200 nm),[7,8] long-lived charge carriers life (at the microsecond level),[9] tunable composition,[10] customizable surface chemistry,[11] and good biocompatibility.[12] These properties have garnered significant research interest in various fields, including optics,[13–15] energy,[16,17] sensing,[18] and biomedicine.[19–21] Unlike traditional luminescent materials with AIE, which suffer from aggregation-induced quenching at high concentrations,[22] limiting their biological applications, AIE-typed luminescent metal NCs exhibit minimal emission in dilute solutions but demonstrate bright emission when concentrated or aggregated.[19,23,24] This unique behavior, coupled with the designability of their surface shell and metal-core, enables the creation of metal NCs with AIE characteristics tailored for specific functions, offering solutions to diverse challenges across multiple domains.

In recent decades, the escalating issue of bacterial resistance due to antibiotic overuse has underscored the urgent need for broad-spectrum, non-resistant antibacterial nanomaterials in public health and environmental hygiene.[25,26] Metal NCs, particularly gold (Au) and silver (Ag) NCs, have shown efficacy in killing a wide range of bacteria without inducing resistance, prompting extensive research in both basic and applied contexts.[27–30] However, their antibacterial mechanism, typically involving self-consumption through metal ion release or cellular internalization to generate reactive oxygen species (ROS), results in a relatively short antibacterial effect.

---

[a] College of Materials Science and Engineering, Qingdao University of Science and Technology (QUST), 53 Zhengzhou Rd., Shibei District, Qingdao 266042, P. R. China. E-mail: yuanxun@qust.edu.cn, zhuhg@qust.edu.cn

[b] Gongtao New Materials Groups, 60 Wuling Rd., Boshan District, Zibo, 255200, China

[c] Department of Hematology, Qingdao Women and Children's Hospital, Qingdao 266011, P. R. China

† Electronic supplementary information (ESI) available. See DOI: https://doi.org/10.1039/d4nr04718d

Recent advancements have demonstrated that AIE-typed Au and AuAg NCs can produce substantial ROS under light irradiation, achieving prolonged and broad-spectrum antibacterial effects.[31–34] Nevertheless, the high cost of Au and Ag limits their widespread application in the antibacterial field. Consequently, developing AIE-typed copper (Cu) NC-based antibacterial agents is of significant interest, given that Cu has similar physicochemical properties to Au and Ag and is a beneficial trace element involved in the synthesis of various proteins and enzymes in the human body.[35–37] On this basis, we hypothesize that designing Cu NCs with AIE characteristics could lead to cost-effective and long-lasting photodynamic sterilization, enhancing their application in antibacterial treatments and wound healing for bacterial infections.

Herein, we report the design of AIE-typed luminescent Cu NCs as photodynamic antibacterial agents to facilitate wound healing in bacterial infections (Scheme 1). The central aspect of this design is the formation of a dense ligand layer composed of cysteine (cys) and chitosan (CS) that is established through strong electrostatic interactions between the protonated amine groups of CS and the deprotonated carboxyl groups of cys by manipulating the reaction pH and temperature. Within this dense ligand layer, Cu(0)@Cu(I)-thiolate NCs are generated *in situ* after the introduction of Cu^{2+}, thereby rapidly producing highly luminescent Cu NCs with AIE characteristics (Cu-cys-CS NCs for short). By manipulating the reaction pH and temperature, the PL of the Cu-cys-CS NCs can be tuned by altering the aggregation degree of the ligand layer. These AIE-typed Cu-cys-CS NCs exhibit suitable HOMO–LUMO positions, strong PL, and long carrier lifetimes, enabling the photoinduced generation of abundant ROS for bacterial elimination. Moreover, the inherent antibacterial activity of CS and Cu further improves the antibacterial efficacy of the AIE-typed Cu-cys-CS NCs. Consequently, the designed Cu-cys-CS NCs demonstrate significant rapid bacterial inactivation under visible light irradiation *in vitro*, along with a favorable wound healing effect *in vivo*. The findings of this study underscore the promising potential of the proposed drug for photodynamic therapy in treating wound infections. This study establishes a foundation for the future development of AIE-typed Cu NCs based on photodynamic antibacterial agents and their application in treating bacterial infection wounds.

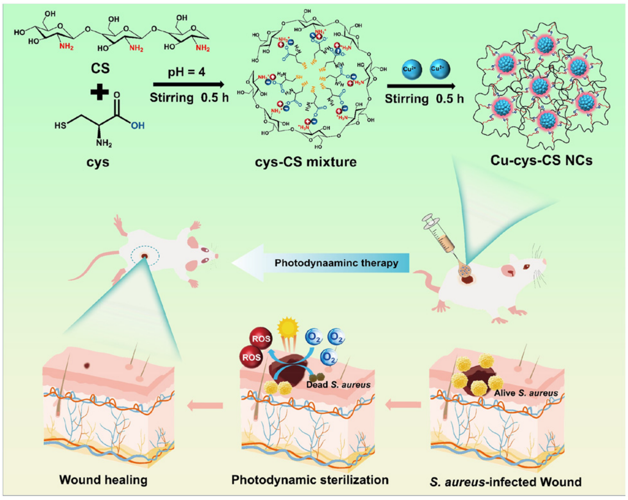

Scheme 1 Schematic representation of AIE-typed Cu-cys-CS NC antibacterial agents for wound healing *via* photodynamic bacteria elimination.

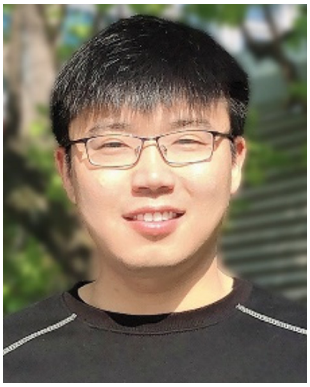

Haiguang Zhu

Dr Haiguang Zhu received his B.S. degree (2013) from Jiangsu University and PhD (2018) from Soochow University, under the co-supervision of Prof. Qingfeng Xu and Prof. Jianmei Lu. He studied at the National University of Singapore (NUS) (2016–2017) as an exchange student under the supervision of Prof. Jianping Xie. He joined Qingdao University of Science and Technology (QUST) in 2018. His research focuses on the synthesis and applications of metal nanoclusters.

2. Experimental section

2.1. Chemicals and materials

Ultrapure water (18.2 MΩ cm) was used throughout the experiment. All glassware was cleansed with aqua regia, thoroughly rinsed with an abundance of ethanol and water, and subsequently dried in an oven before use. Copper nitrate trihydrate ($Cu(NO_3)_2 \cdot 3H_2O$), cysteine (cys), and chitosan (CS) were purchased from Adamas Reagent Co., Ltd. Chitosan had a degree of deacetylation of ≥90%, a viscosity of ≤100 mPa s, and a molecular weight ranging from approximately 50 kDa to 100 kDa. The 2′,7′-dichlorofluorescein diacetate (DCFH-DA) dye and dimethyl sulfoxide (DMSO) were obtained from Sinopharm Chemical Reagent Co., Ltd. Formalin solution was purchased from Merck. Phosphate buffer solution (PBS) solution, Luria–Bertani (LB) nutrient agar, and LB broth were purchased from Qingdao Hope Bio-Technology Co., Ltd. Vancomycin hydrochloride (Van) and carbomer were purchased from Shanghai McLean Biochemical Co., Ltd. A complete Dulbecco's modified Eagle's medium (DMEM) was purchased from Beijing Solarbio Science & Technology Co., Ltd. Standard strains of *Staphylococcus aureus* ATCC 6538 (*S. aureus*), *Escherichia coli* ATCC 25922 (*E. coli*), and *C. albicans* were purchased from China General Microbiological Culture Collection Center. L929 mouse fibroblast cells were purchased from the American Type Culture Collection. Female ICR mice aged six weeks were procured from China Weitonglihua Animal Co., Ltd. The animals were housed under specific pathogen-free conditions. All animal experiments were conducted following "International Ethical Guidelines" and the "NIH Guide for the Care and Use of Laboratory Animals".

2.2 Instrumentation

The spectral absorption characteristics of diverse samples, along with the turbidity measurements in microbiology, were meticulously examined utilizing a Shimadzu UV-1800 spectrophotometer. Steady-state and time-resolved PL spectra were acquired employing a PerkinElmer LS-55 fluorescence spectrometer and a dedicated time-resolved PL system (FLS-1000), respectively. The size of Cu-cys-CS NCs was meticulously inspected *via* transmission electron microscopy (TEM, JEM-2100 Plus). The morphology of bacteria was observed using a scanning electron microscope (SEM, JSM-6700F). UV–visible diffuse reflectance (DRS) spectra were recorded on a U-3900 spectrophotometer with an integration sphere. Fourier transform infrared (FTIR) spectroscopy, spanning the range of 4000 to 450 cm^{-1}, was conducted on a Horiba-Jobin Yvon FluoroMax-4 spectrophotometer. X-ray photoelectron spectroscopy (XPS) and valence band XPS (VB-XPS) data were gathered on an ESCALAB MK II Axis Ultra DLD system, utilizing Al Kα radiation as the excitation source, with the spectrometer and work function calibrated to the C 1s peak at 284.8 eV. The specific types of reactive oxygen species (ROS)-singlet oxygen ($^1O_2$), superoxide anions ($^{\bullet}O_2^-$), and hydroxyl radicals ($^{\bullet}OH$)-were measured using an electron paramagnetic resonance (EPR) spectrometer (EPR200-Plus, China). The production of H_2O_2 over Cu-cys-CS NCs was determined using a colorimetric method. In this procedure, 1 mL of a 2,9-dimethyl-1,10-phenanthroline (DMP) ethanol solution (10 mg mL^{-1}) and 1 mL of a 0.01 M $CuSO_4$ aqueous solution were added to a centrifuge tube. Subsequently, 0.5 mL of the reaction solution and 0.5 mL of isopropanol were combined in the tube. The mixture was then incubated at room temperature for 10 minutes, after which the absorbance of the resulting solution was analyzed using a UV-2600 UV–Vis spectrophotometer (Shimadzu). The production of H_2O_2 was quantified by measuring the absorbance of the supernatant at 454 nm. Dynamic light scattering (DLS) measurements were carried out on a NanoBrook Omni from Brookhaven Instruments.

2.3 Preparation of CS solution

30 mg of CS was added to 6 mL of water, followed by introducing a few drops of ice-cold acetic acid (99%–100%) while continuously stirring to facilitate CS dissolution. The pH of the dissolved CS solution was around 3.2. Subsequently, the pH of the solution was adjusted to around 5.2 using 1 M NaOH.

2.4 Synthesis of AIE-typed luminescent Cu-cys-CS NCs

1 mL of cys solution (30 mg mL^{-1}) and 0.5 mL of CS (5 mg mL^{-1}) were introduced into 2.44 mL of ultrapure water, followed by stirring at room temperature for 30 minutes. Subsequently, 60 μL of $Cu(NO_3)_2$ (0.3 M) was added to the mixed solution and stirred for 30 minutes at room temperature to obtain highly luminescent Cu-cys-CS NCs. Finally, the obtained solution was stored in a refrigerator at 4 °C for further use.

2.5 Antimicrobial experiments of AIE-typed luminescent Cu-cys-CS NCs

Gram-negative *E. coli*, Gram-positive *S. aureus*, and *Candida albicans* (*C. albicans*) were selected as the microbial model to evaluate the antimicrobial effectiveness of Cu-cys-CS NCs. All glassware and culture media were sterilized, and antimicrobial experiments were performed under aseptic conditions. Bacterial cells were cultured in the LB medium at 37 °C for 18 hours, followed by centrifugation at 8000 rpm to remove metabolites. The cells were then diluted with PBS solution (0.01 M, pH 7.4) to prepare a bacterial suspension with a concentration of 10^7 CFU mL^{-1} ($OD_{600} \approx 0.1$). In a typical antimicrobial experiment, 1 mL of Cu-cys-CS NCs (0.5 mM) was mixed with 4 mL of the microbial suspension, while for the control group, 1 mL of PBS solution was mixed with 4 mL of the microbial suspension. Both the control and experimental groups were then exposed to a 300 W xenon lamp (equipped with the commercial optical cut-off filter UVCUT 400, $\lambda \geq 400$ nm), Beijing China Education AuLight Technology (CEAuLight) Co., Ltd with a light intensity of 100 mW cm^{-2} for 40 minutes. Every 20 minutes, 100 μL of the mixture was taken, diluted 1000-fold, and smeared onto fresh agar plates, which were subsequently incubated at 37 °C for 24 hours to count the colonies and determine the number of viable bacteria. Additional antimicrobial experiments were conducted in the absence of light.

2.6 ROS assay

The intracellular ROS levels were qualitatively assessed using 2′,7′-dichlorofluorescein diacetate (DCFH-DA), a cell-permeable nonfluorescent molecular probe oxidized by ROS to produce fluorescent 2′7′-dichlorofluorescein (DCF). Initially, 4 mL of the bacterial solution was mixed with 1 mL of the Cu-cys-CS NCs antimicrobial agent and 40 μL (200 μM) of DCFH-DA. Subsequently, the mixture was irradiated under visible light ($\lambda \geq 400$ nm, 100 mW cm^{-2}) for 1 h. After that, 1 mL of the mixture was centrifuged at 8000 rpm for 5 minutes, and the supernatant was discarded. The pellet was washed three times with PBS by centrifugation and then reconstituted to a final volume of 1 mL. The fluorescence intensity of DCF at a wavelength of 525 nm was measured at an excitation wavelength of 488 nm using a fluorescence spectrophotometer to assess the ROS content.

2.7 Cytotoxicity test

The cytotoxicity of the Cu-cys-CS NC antimicrobial agent was assessed using a cell proliferation kit (MTT), with L-929 cells serving as the model. Initially, the L-929 cells were seeded in a 96-well plate at a concentration of 10^4 cells per well and cultured under standard conditions (37 °C, 5% CO_2) for 24 hours. Subsequently, various concentrations of the antimicrobial agent were added to each well, which were then exposed to visible light for 40 minutes. Following this incubation, 20 μL of MTT solution was added to each well, and the cells were cultured for an additional 4 hours in the incubator. After this period, the culture medium was removed, and 150 μL of DMSO was added to each well. The plates were allowed to stand for 30 minutes, after which the absorbance at 570 nm was measured using a Tecan Spark® multimode microplate reader.

2.8 Animal experiments

Mice were randomly assigned to six groups, each consisting of three individuals: the uninfected group, the carbomer group, the carbomer + Light group, the Cu-cys-CS NCs (dispersed in carbomer) group, the Cu-cys-CS NCs (dispersed in carbomer) + Light NCs group, and the Van group. The mice were anesthetized with an appropriate dose of isoflurane (2%), and hair was removed from a designated area on their backs using a depilatory cream. Full-thickness wounds were created on the dorsal skin using an 8 mm diameter skin biopsy punch. 100 μL suspension of *S. aureus* (10^8 CFU mL^{-1}) was inoculated at the wound site, which was then covered with a 3 M film and left undisturbed for one day to facilitate infection development.

Following this, the infected wounds were treated with 200 μL of various photodynamic antimicrobial agents (0.1 mM, dispersed in carbomer). The wound sites were irradiated daily for 5 minutes using a xenon lamp light source equipped with a 400 nm optical cut-off filter. After a treatment duration of nine days, all mice were euthanized, and the surrounding wound tissues were fixed using 4% paraformaldehyde for subsequent H&E staining. Blood samples were also collected for the analysis of inflammatory factors, including tumor necrosis factor-alpha (TNF-α), interleukin-1 beta (IL-1β), and interleukin-6 (IL-6).

3. Results and discussion

3.1. Synthesis and characterization of AIE-typed luminescent Cu-cys-CS NCs

In this study, AIE-typed luminescent Cu-cys-CS NCs were synthesized in the presence of CS and cys (for detailed procedures, see the Experimental section). As illustrated in Fig. 1a, the as-synthesized Cu-cys-CS NC solution appears pale yellow (item 1) with good visible light absorption across the wavelength range of 400 nm to 600 nm (black curve). This observation implies the formation of ultrasmall Cu NCs (<3 nm), rather than larger copper nanoparticles, which typically exhibit surface plasmon resonance absorption between 550 nm and 600 nm.[38] The DLS results indicated that the aggregates formed by CS polymers and cys molecules have a particle size of approximately 340 nm (Fig. S1†). Additionally, TEM imaging provided direct evidence, revealing small particles approximately 1.8 nm in size encapsulated within the aggregates formed by the CS polymers and cys molecules (Fig. 1b). Furthermore, the as-synthesized Cu-cys-CS NCs emit intense red PL (item 2 in the inset of Fig. 1a), with an emission peak at 621 nm (red curve, excited at 365 nm), suggesting a substantial Stokes shift exceeding 200 nm. This large Stokes shift highlights the characteristic AIE behavior of Cu-cys-CS NCs and indicates that the luminescence originates primarily from the relaxation processes of ligand-to-metal charge transfer (LMCT) or ligand-to-metal–metal charge transfer (LMMCT). This is further evidenced by the time-resolved PL spectrum of Cu-cys-CS NCs. This spectrum reveals two components (Fig. 1c): a low proportion τ_1 (0.15 μs, 23%), stemming from the interband transition (d ← sp) of the metal core, and a high contribution τ_2 (77%), arising from LMCT or LMMCT. Notably, the PL lifetime of Cu-cys-CS NCs is up to 1.77 μs, surpassing the lifetimes of most non-AIE metal NCs (typically in the picosecond or nanosecond range). Additionally, the PL quantum yield of the Cu-cys-CS NCs is found to be 5.1% at a concentration of 1.125 mM. Consequently, the combination of effective visible light harvesting, strong PL output, large Stokes shift, and long-lived PL lifetime in AIE-typed Cu NCs positions them as highly suitable candidates for efficient photodynamic antibacterial activities and wound healing applications.

The surface chemistry of AIE-typed luminescent Cu-cys-CS NCs was further characterized using FTIR. The characteristic stretching vibration of the -SH bond at 2548 cm^{-1} was not observed in the FTIR spectrum of Cu-cys-CS, in contrast to the cys sample, which could be attributed to the attachment of cys molecules to the Cu core *via* Cu–S bonds (Fig. 1d).[39] Meanwhile, this interaction likely alters the structure of cys, as indicated by the disappearance of the vibration band at 2078 cm^{-1}. This band is associated with the deformation of the asymmetrical vibration of the amine groups ($-NH_2$) caused by the vibration of carboxyl groups (–COOH).[40] Additionally, the FTIR spectrum of Cu-cys-CS NCs closely resembles that of CS, indicating that Cu-cys-CS NCs and CS share similar surface properties. Furthermore, zeta potential measurements for Cu-cys-CS NCs and CS yielded similar values, reinforcing the presence of the CS polymer coating on the surface of Cu-cys-CS NCs (Fig. 1e). Moreover, XPS analysis was conducted to investigate the valence states of the Cu elements in Cu-cys-CS NCs. Fig. 1f displays two peaks at 932.3 eV and 951.8 eV, corresponding to the binding energies of Cu $2p_{3/2}$ and Cu $2p_{1/2}$ electrons of Cu(0), respectively. Notably, the difference in binding energy between Cu(0) and Cu(I) for the Cu $2p_{3/2}$ state is approximately 0.1 eV. This indicates that the valence state of the AIE-typed Cu NCs is likely situated between 0 and +1, confirming the coexistence of both Cu(I) and Cu(0) within the Cu-cys-CS NCs.[41,42] Furthermore, the binding energy for Cu(II) at 942.5 eV was not detected in the Cu 2p spectrum, suggesting that Cu(II) has been reduced by cys.

After confirming the successful preparation of AIE-typed luminescent Cu-cys-CS NCs, the underlying PL mechanism was investigated. Initially, we explored the effects of cys and CS on the PL properties of Cu-cys-CS NCs. As illustrated in Fig. S2,† the synthesis solution without added CS shows no significant absorption in the visible light region and does not produce an emission peak under UV excitation, indicating an absence of luminescence properties (Fig. S2a and b†).

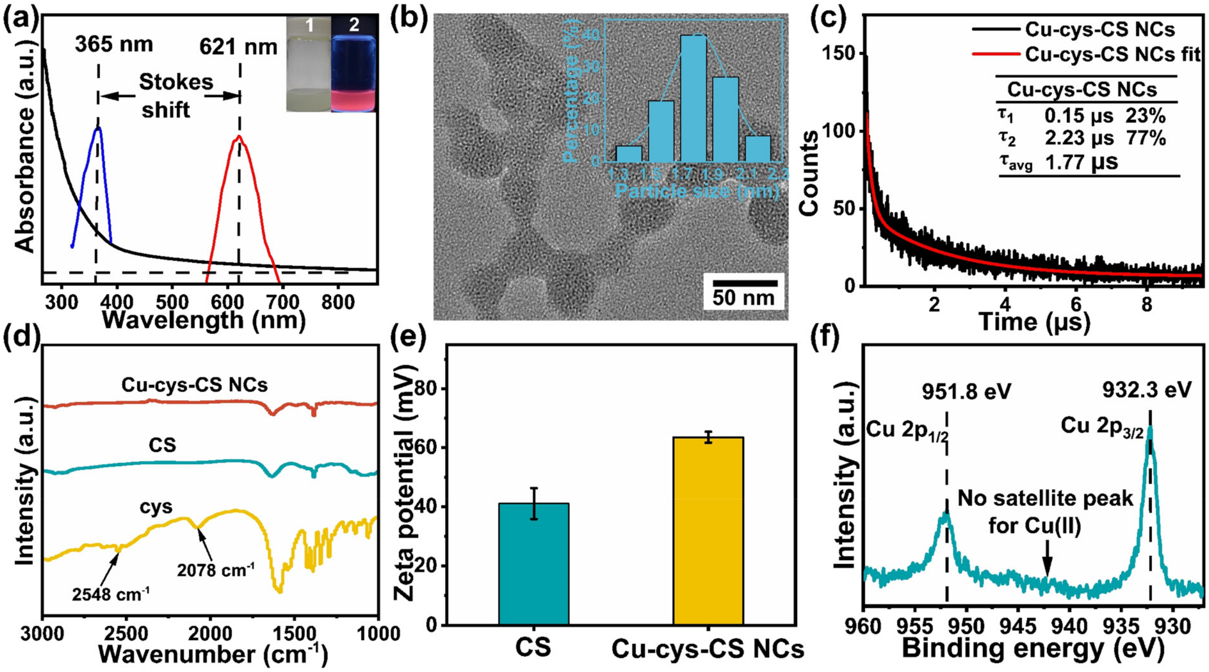

Fig. 1 (a) UV–visible absorption (black curve), photoexcitation (blue curve), and photoemission spectra (red curve) of Cu-cys-CS NCs (inset: the optical images of Cu-cys-CS NC solution under visible light illumination (item 1) and UV illumination (item 2)). (b) Representative TEM image and size distribution histogram (inset) of Cu-cys-CS NCs. (c) Time-resolved PL decay profile and the corresponding fit curve of Cu-cys-CS NCs. (d) FTIR spectra of Cu-cys-CS NCs, CS polymers, and cys molecules. (e) Zeta potential result of Cu-cys-CS NCs and CS. (f) High-resolution XPS of Cu 2p in Cu-cys-CS NCs.

Similarly, the omission of cys results in poor light absorption and a lack of PL. These findings highlight the crucial synergistic interaction between CS and cys in enhancing the luminescence properties of Cu-cys-CS NCs (Fig. S2c and d†). Furthermore, we optimized the amount of CS used in the synthesis. With a fixed quantity of cys, we found that when 2.5 mg of chitosan was used, the PL intensity of Cu-cys-CS NCs reached their peak (Fig. S3†). This can likely be attributed to the formation of the densest structure between CS and cys under these conditions, resulting in the highest PL observed in the solution.

The influence of pH and temperature of the synthesis medium on the PL properties of Cu-cys-CS NCs were investigated, as these factors are critical in determining the interactions between cys and CS and, consequently, the PL properties of the NCs. Fig. 2a–c depicts the PL intensities of Cu-cys-CS NCs synthesized under varying pH values (3.5, 4, 4.5, 5, 5.5, and 6). The data reveal that the PL intensity peaks at pH 4, while further increases in pH lead to significant fluorescence quenching. At pH 6, the NCs exhibit almost no PL. This behavior is primarily attributed to the protonation and deprotonation of $-NH_2$ on CS and –COOH on cys, which depend on the pH of the surrounding solution. The pK_a value of $-NH_2$ on CS is typically around 6.5 (Fig. S4a†); thus, at pH 4, the $-NH_2$ groups bind to an H^+, becoming positively charged ($-NH_3^+$). Conversely, the pK_a value of the –COOH groups on cys is approximately 1.92 (Fig. S4b†); at pH 4, these groups lose an H^+, becoming negatively charged (–COO–). As a result, the positively charged CS and negatively charged cys aggregate through strong electrostatic interactions (Fig. 2d), which enhance the rigidity of the capping ligands and reduce the likelihood of non-radiative relaxation of the excited state, ultimately improving the PL properties of Cu-cys-CS NCs. The reduced PL intensity at pH 6 can be attributed to the proximity of the pK_a value of CS, which leads to CS deprotonation and a subsequent weakening of the electrostatic interactions between CS and cys.

Fig. 2e illustrates the PL intensities of Cu-cys-CS NCs synthesized at different temperatures. Contrary to previous findings suggesting that an increased temperature enhances the aggregation of coating ligands,[8] thereby improving the PL intensity, our results indicate that the PL intensity of Cu-cys-CS NCs decreases as the reaction temperature increases. This decrease is primarily due to intensified intermolecular motion at elevated temperatures, which weakens the electrostatic interactions between chitosan and cys. Consequently, the synergistic effects of CS and cys are pivotal in the synthesis of AIE-type luminescent Cu-cys-CS NCs at room temperature. The room temperature synthesis conditions offer a more flexible and low-energy strategy for the preparation of AIE-typed luminescent Cu NCs, further enhancing their prospective applications in real life.

3.2. Photodynamic antibacterial tests *in vitro*

After confirming the successful synthesis of AIE-typed luminescent Cu-cys-CS NCs, we investigated their photodynamic

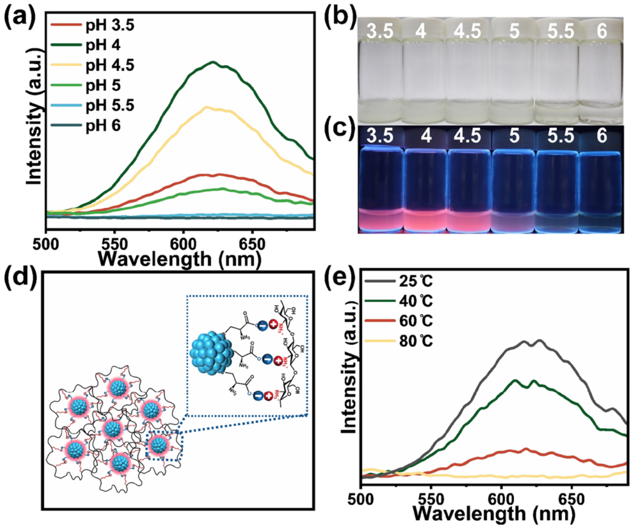

Fig. 2 (a) The photoemission spectra of Cu-cys-CS NCs synthesized under varying pH values. The optical images of the Cu-cys-CS NCs synthesized under varying pH values under visible light illumination (b) and UV illumination (c). (d) Schematic illustration of the AIE-typed Cu-cys-CS NCs coordinated by CS and cys *via* strong electrostatic interaction. (e) The photoemission spectra of Cu-cys-CS NCs synthesized under different temperatures.

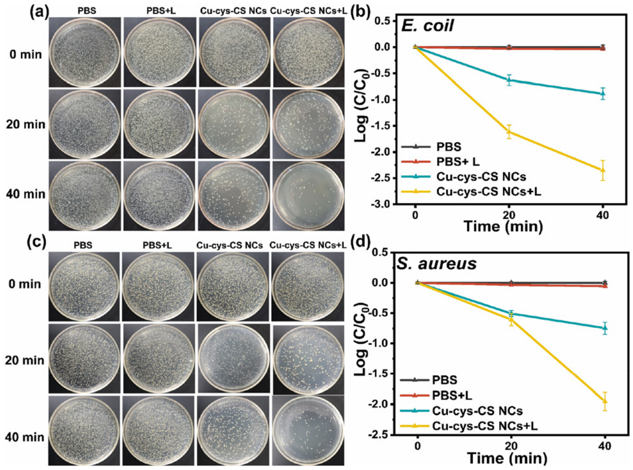

Fig. 3 Bacterial colony growth (a and c) and quantitative analysis in bacterial viability (b and d) of Gram-negative *E. coli* (a and b) and Gram-positive *S. aureus* (c and d) treated with Cu-cys-CS NCs under the conditions of visible-light illumination for 40 minutes, and those reference groups treated with Cu-cys-CS NCs under dark conditions and without antibacterial agents under the dark conditions or visible-light illumination.

antibacterial performance under visible light irradiation ($\lambda \geq$ 400 nm, 100 mW cm^{-2}). Gram-negative *E. coli* and the Gram-positive *S. aureus* were chosen as two representative bacteria. As illustrated in Fig. 3, AIE-typed luminescent Cu-cys-CS NCs effectively eliminated 99.52% of *E. coli* with a 2.3 order of magnitude reduction in colony-forming units (CFU) (Fig. 3a and b) and 98.89% of *S. aureus* with a reduction of 2.0 orders of magnitude in CFU (Fig. 3c and d) within 40 minutes. These results demonstrate the superior photodynamic bacterial elimination performance of AIE-typed luminescent Cu-cys-CS NCs. In contrast, control experiments without the addition of Cu-cys-CS NCs under light illumination (PBS + L) showed no significant impact on bacterial elimination, indicating that visible light irradiation alone has a negligible effect on bacterial growth. Additionally, approximately 0.8 orders of magnitude reduction in CFU of *E. coli* and 0.7 orders of magnitude reduction in CFU of *S. aureus* were achieved by Cu-cys-CS NCs in the absence of light exposure, leading to two important conclusions: (i) AIE-typed luminescent Cu-cys-CS NCs have inherent intrinsic antimicrobial properties under dark conditions; (ii) the photodynamic antimicrobial performance of AIE-typed luminescent Cu-cys-CS NCs is enhanced and the underlying mechanism will be discussed later. Furthermore, AIE-typed luminescent Cu-cys-CS NCs also demonstrated excellent antifungal activity against *C. albicans* (94.60%) under visible light irradiation, achieving a reduction of 1.3 orders of magnitude in CFU (Fig. S5†), which underscores the potential to broaden the application fields for AIE-typed luminescent Cu-cys-CS NCs. Overall, these findings suggest that AIE-typed luminescent Cu-cys-CS NCs exhibit remarkable photodynamic antimicrobial activities, positioning them as promising agents for the treatment of bacteria-infected wounds.

3.3. The antibacterial mechanism of the AIE-typed luminescent Cu-cys-CS NCs

To further elucidate the underlying mechanism behind the excellent visible-light-driven antibacterial activity of AIE-typed luminescent Cu-cys-CS NCs, we first evaluated their optical absorption using UV-visible DRS, which is essential for photodynamic antibacterial function. The UV-visible DRS curve (Fig. 4a) and the corresponding Kubelka–Munk plots (inset of Fig. 4a) indicate that Cu-cys-CS NCs exhibit good visible light

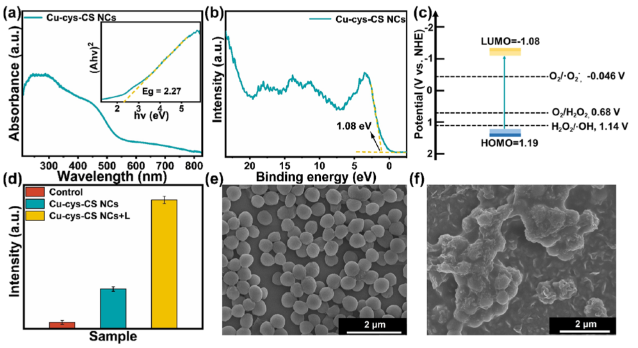

Fig. 4 (a) UV-visible DRS spectrum of Cu-cys-CS NCs (inset: the corresponding Kubelka–Munk plots). (b) VB-XPS spectrum of Cu-cys-CS NCs. (c) The diagram of energy levels of Cu-cys-CS NCs. (d) The PL intensity of DCF treated with PBS under dark conditions (control group), and treated with Cu-cys-CS NCs in the absence or presence of light treatments. SEM images of the *S. aureus* before (e) and after (f) photodynamic antibacterial test.

absorption, attributable to their relatively narrow energy bandgap (E_g, 2.27 eV). This characteristic helps explain their effective photodynamic bacterial elimination performance under visible light illumination.

Considering that reactive oxygen species (ROS), including superoxide (O_2^-), hydroxyl radicals ($^\bullet OH$), and hydrogen peroxide (H_2O_2)—play a crucial role in bacterial inactivation, we assessed the positions of the highest occupied molecular orbital (HOMO) and the lowest unoccupied molecular orbital (LUMO) of Cu-cys-CS NCs. These measurements are critical for determining the photodynamic generation of ROS. As shown in Fig. 4b, the VB position of Cu-cys-CS NCs is calculated to be 1.08 V by valence band X-ray photoelectron spectroscopy (VB-XPS). According to the following equation:

$$E_{\mathrm{RHE}} = \varphi + E_{\mathrm{VB\text{-}XPS}} - 4.44$$

where E_{RHE} is the reversible hydrogen electrode (RHE) potential, φ is the electron work function of the instrument (4.55) and $E_{\mathrm{VB\text{-}XPS}}$ is the VB energy. The VB position (corresponding to the HOMO) of Cu-cys-CS NCs is converted into the electrochemical energy potentials in volts of 1.19 V *vs.* RHE (pH = 0). Given the E_g value of Cu-cys-CS NCs, the conduction band (CB) level, corresponding to the LUMO, was calculated to be −1.08 eV relative to RHE (pH = 0), which is more negative than the reduction potentials for O_2 ($O_2/^\bullet O_2^-$, −0.046 V *vs.* RHE; (pH = 0) O_2/H_2O_2, 0.68 V *vs.* RHE (pH = 0)). These conditions indicate a thermodynamically favorable pathway for producing $^\bullet O_2^-$ and H_2O_2 through O_2 reduction (Fig. 4c). Moreover, the VB level of Cu-cys-CS NCs exceeds the potentials for H_2O_2 to generate $^\bullet OH$ ($H_2O_2/^\bullet OH$, 1.14 V *vs.* RHE (pH = 0)), facilitating the oxidation of H_2O_2 to produce $^\bullet OH$.

To assess the ROS levels in bacteria treated with various samples, we employed 2′,7′-dichlorofluorescein diacetate (DCFH-DA), which can be oxidized by the ROS to yield fluorescent 2′,7′-dichlorofluorescein (DCF). The PL intensity of DCF generated in bacteria treated with Cu-cys-CS NCs under visible light illumination was significantly higher than that of the other groups, indicating the highest ROS production associated with Cu-cys-CS NCs and confirming their strong photodynamic antibacterial activity (Fig. 4d). To further confirm the specific types of ROS produced, we conducted EPR spectroscopy to detect $^1O_2$, $^\bullet O_2^-$, and $^\bullet OH$ during the photocatalytic reaction. The EPR signal of the adduct DMPO-$^\bullet$OH was observed under visible light illumination, while no signals for $^\bullet O_2^-$ and $^1O_2$ were detected under the same conditions (Fig. S6a–c†). These results indicate that Cu-cys-CS NCs are capable of producing $^\bullet OH$ while excluding the generation of $^\bullet O_2^-$ through one-electron O_2 reduction and $^1O_2$ *via* energy transfer. Furthermore, the engineered Cu-cys-CS NCs demonstrated the capacity to produce H_2O_2, which can react with DMP and $CuSO_4$ to form the Cu(I)-DMP complex, characterized by a prominent peak at 454 nm (Fig. S6d†). Based on these findings, we concluded that $^\bullet OH$ and H_2O_2 are the primary ROS species responsible for bactericidal activity, with H_2O_2 likely produced through a two-electron reduction of O_2 and $^\bullet OH$ generated *via* the oxidation of H_2O_2.

It is noteworthy that Cu-cys-CS NCs can also induce ROS generation in bacteria even in the absence of visible light, likely attributable to the inherent antimicrobial properties of the CS polymers and Cu species that induce oxidative stress in the bacteria. This underpins the observed antibacterial activity of Cu-cys-CS NCs under dark conditions. Furthermore, SEM was used to observe the morphologies of bacteria before and after photodynamic bactericidal treatment, revealing significant morphological changes in *S. aureus*, which transitioned from a plump, smooth, and intact state to one that was collapsed, wrinkled, and cracked (Fig. 4e and f). These morphological alterations can be ascribed to the destruction and oxidation of the bacterial cell membrane by ROS, ultimately leading to bacterial inactivation.

3.4 *In vivo* wound healing assessment

Building on the remarkable photodynamic antibacterial activity of AIE-Cu-cys-CS NCs, we investigated their therapeutic effects on *S. aureus*-infected wounds (Fig. 5a). Initially, we assessed the cytotoxicity of Cu-cys-CS NCs towards L929 cells before conducting the wound healing experiments. As demonstrated in Fig. S7,† L929 cells exhibited good viability (86.1%) after a 24-hour treatment with Cu-cys-CS NCs, indicating low cytotoxicity. This can be attributed to the natural biocompatibility of CS and cys, as well as the low toxicity of Cu species. The wound-healing process was documented using a digital

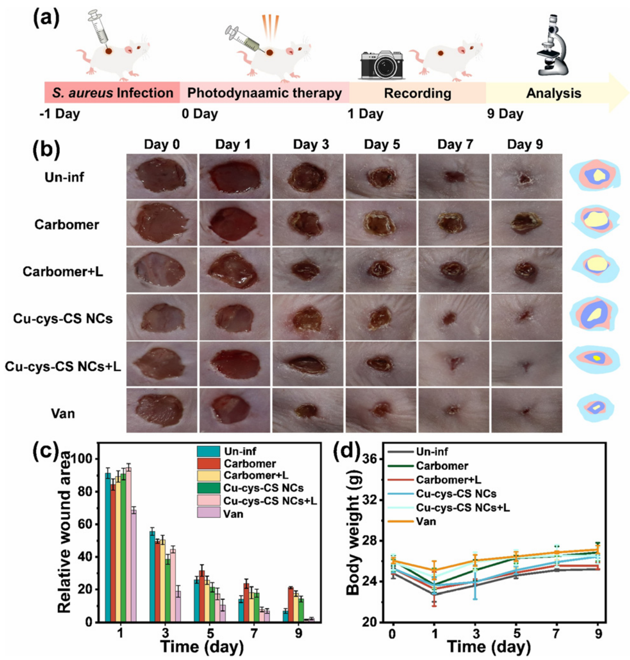

Fig. 5 (a) Schematic illumination of *S. aureus* infected wound healing. (b) Representative images of the *S. aureus* infected wounds treated with various antibacterial agents at the determined time and the simulation images of wound areas on days 1, 3, 5 and 9 in different groups. The Un-inf group represents uninfected skin wounds. (c) Representative wound size changes from day 1 to day 9. (d) Representative weight changes of different groups from day 1 to day 9 during the treatment.

camera. Fig. 5b and c illustrate that all *S. aureus*-infected wounds began to show signs of healing by day 3 post-treatment with a significant reduction in the wound area. Notably, the body weights of mice treated with Cu-cys-CS NCs + light (Cu-cys-CS NCs + L) and Van recovered back to those before the disease (Fig. 5d), signifying effective control of bacterial infection due to the superior photodynamic antibacterial activity of Cu-cys-CS NCs. By day 7, we measured the wound sizes of mice treated with Carbomer, Carbomer + light (Carbomer + L), Cu-cys-CS NCs, Cu-cys-CS NCs + light (Cu-cys-CS NCs + L), and Van as 23.6 ± 2.8, 18.1 ± 3.5, 17.8 ± 2.36, 7.9 ± 1.4 and 6.9 ± 1.4 respectively, with corresponding wound healing rates of 76.4%, 81.9%, 82.2%, 92.1%, 93.1%. By day 9, the *S. aureus*-infected wounds treated with Cu-cys-CS NCs under visible light irradiation and Van had fully healed, resulting in the regeneration of new epidermal tissue, while the wounds treated with the other samples still presented scabs, with unhealed areas of 7.1%, 21.2%, 17.6%, and 14.4%, respectively. Furthermore, Cu-cys-CS NCs exhibited similar therapeutic effects with Van, a commercial antibacterial agent. However, the broad-spectrum antibacterial activity, multiple antibacterial mechanisms, and resistance inhibition of the AIE-typed Cu-cys-CS further highlighted their significant potential for clinical applications. These results suggest that Cu-cys-CS NCs can generate ROS under visible light irradiation to eradicate bacteria, ultimately facilitating the healing of infected wounds.

The processes of skin remodeling and regeneration play a critical role in wound treatment and were assessed using hematoxylin and eosin (H&E) as well as Masson staining. The infected wound tissues treated with AIE-typed luminescent Cu-cys-CS NCs + light displayed excellent repair, evidenced by the complete recovery of epidermal and dermal structures in H&E staining (Fig. 6a). In contrast, wound tissues from the Carbomer, Carbomer + L, and Cu-cys-CS NCs groups remained severely damaged. These findings align with the observed wound repair results. Moreover, we detected almost no inflammatory cells in the infected wounds treated with Cu-cys-CS NCs under light irradiation, while some inflammatory cells were still present in the other groups (indicated by yellow arrows in Fig. 6). The collagen content, an important indicator of the transition from the inflammatory phase to the recovery phase, was assessed *via* Masson staining. The wounds in the AIE-typed luminescent Cu-cys-CS NCs + L group displayed a high collagen content (blue area) with orderly arranged and dense structures, closely resembling that in the uninfected control group (Fig. 6b). Conversely, the collagen in the other treatment groups was found in a degraded state due to the action of collagenase secreted by bacteria. Additionally, the expression levels of pro-inflammatory factors in infected wounds, including tumor necrosis factor-alpha (TNF-α, Fig. 6c), interleukin-1 beta (IL-1β, Fig. 6d), and interleukin-6 (IL-6, Fig. 6e), are in good agreement with the therapeutic effects in different groups. These results indicate that AIE-typed luminescent Cu-cys-CS NCs could effectively eradicate bacteria under light conditions, reducing the levels of inflammatory factors, while promoting the formation of new collagen, thereby accelerating skin remodeling and regeneration of infected wounds. Additionally, Cu-cys-CS NCs under light irradiation demonstrated therapeutic effects comparable to those of Van, as evidenced by similar results in H&E staining, Masson staining, and the expression levels of inflammatory factors, further highlighting the potential of Cu-cys-CS NCs for clinical applications.

Following the treatment experiments, the mice were euthanized, and their main organs (heart, liver, spleen, lungs, and kidneys) were dissected to assess the biocompatibility of Cu-cys-CS NCs. Histopathological evaluation of the organs in each group, using H&E staining (Fig. 7), revealed no significant differences, indicating that Cu-cys-CS NCs did not cause any damage to the major organs.

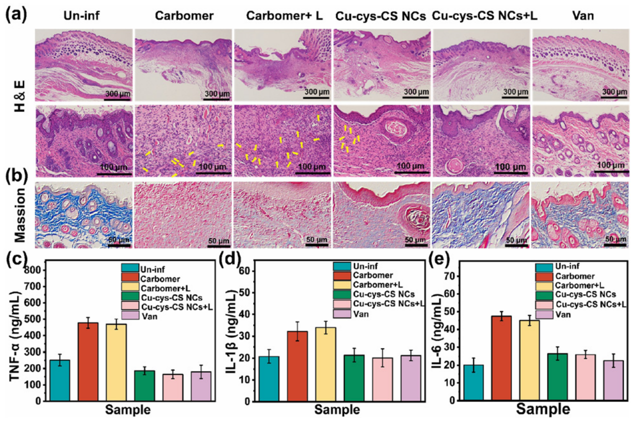

Fig. 6 (a) Representative H&E staining images of tissue slices treated with different samples on day 9 (yellow arrows refer to the inflammatory cells). (e) Representative (b) Masson staining images of tissue slices treated with different samples on day 9 (the blue area represents the collagen fiber). The expression levels of TNF-α (c) IL-1β (d), and IL-6 (e) in blood treated with different samples on day 9.

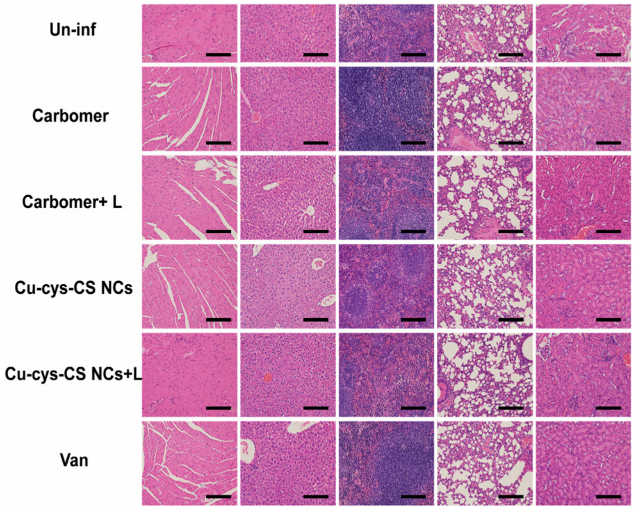

Fig. 7 H&E-stained histological imaging of the heart, liver, spleen, lungs, and kidneys in mice treated with different samples (scale bar = 300 μM).

4. Conclusion

In conclusion, we have successfully developed an antibacterial agent based on AIE-typed luminescent Cu NCs by manipulating the pH and temperature of the reaction solutions. This process enhanced the aggregation degree of the ligand layers, leading to the production of highly luminescent Cu NCs. The AIE characteristics, such as excellent PL, large Stokes shift, and long charge carrier life, enable these Cu NCs to generate substantial amounts of ROS under visible light irradiation, effectively killing bacteria. Furthermore, the intrinsic antimicrobial properties of CS polymers and Cu species contribute to inducing oxidative stress in bacteria. Consequently, the AIE-typed Cu NCs demonstrated significant photodynamic antibacterial efficacy against various microbial pathogens *in vitro*. They also showed promising results in treating bacteria-infected wounds, promoting collagen growth, and reducing inflammation. Additionally, the Cu NCs exhibited favorable biocompatibility due to the natural biocompatibility of CS and cys. The strategy and design outlined in this study may inspire further development of AIE-typed luminescent Cu NC-based photodynamic antibacterial agents for the healing of bacteria-infected wounds.

Author contributions

Zhen Jiang: methodology, formal analysis, investigation, data curation, and writing – original draft. Yongqi Wei: validation and software. Yun Wang: validation and resources. Songjie Han: validation and investigation. Ze Li: validation and investigation. Sihang Liu: validation, visualization, and investigation. Zihao Wang: visualization and investigation. Zhijun Li: conceptualization. Ting Feng: funding acquisition. Haiguang Zhu: conceptualization, methodology, supervision, funding acquisition, and writing – review & editing. Xun Yuan: conceptualization, methodology, supervision, funding acquisition, and writing – review & editing.

Ethics statement

This study was performed in strict accordance with the NIH guidelines for the care and use of laboratory animals (NIH Publication No. 85-23 Rev. 1985) and was approved by the Biomedical Ethics Committee of Qingdao Zhong Hao Biological Engineering Co., Ltd (Qingdao, China).

Data availability

The data that support the findings of this study are available on request from the corresponding author (Haiguang Zhu), upon reasonable request.

Conflicts of interest

There are no conflicts to declare.

Acknowledgements

This work was supported by the National Natural Science Foundation of China (22071127 and 22371153), the Shandong Province Natural Science Foundation (ZR2024JQ002 and ZR2024QE020), and the Youth Innovation Team Development Program of Shandong Higher Education Institutions (2022KJ155).

References

1 Y. Wang, Z. Liu, A. Mazumder, C. G. Gianopoulos, K. Kirschbaum, L. A. Peteanu and R. Jin, *J. Am. Chem. Soc.*, 2023, **145**, 26328–26338.
2 Y. Zhong, J. Zhang, T. Li, W. Xu, Q. Yao, M. Lu, X. Bai, Z. Wu, J. Xie and Y. Zhang, *Nat. Commun.*, 2023, **14**, 658.
3 X. Kang and M. Zhu, *Chem. Soc. Rev.*, 2019, **48**, 2422–2457.
4 C. Yao, C. Xu, I. Park, M. Zhao, Z. Zhu, J. Li, X. Hai, H. Fang, Y. Zhang, G. Macam, J. Teng, L. Li, Q. Xu, F. Chuang, J. Lu, C. Su, J. Li and J. Lu, *Angew. Chem., Int. Ed.*, 2020, **59**, 8270–8276.
5 X. Kang, S. Wang, Y. Song, S. Jin, G. Sun, H. Yu and M. Zhu, *Angew. Chem., Int. Ed.*, 2016, **55**, 3611–3614.
6 P. P. Sun, B. L. Han, H. G. Li, C. K. Zhang, X. Xin, J. M. Dou, Z. Y. Gao and D. Sun, *Angew. Chem., Int. Ed.*, 2022, **61**, e202200180.
7 X. Kang, S. Wang and M. Zhu, *Chem. Sci.*, 2018, **9**, 3062–3068.
8 Z. Luo, X. Yuan, Y. Yu, Q. Zhang, D. T. Leong, J. Y. Lee and J. Xie, *J. Am. Chem. Soc.*, 2012, **134**, 16662–16670.
9 Y. E. Shi, J. Ma, A. Feng, Z. Wang and A. L. Rogach, *Aggregate*, 2021, **2**, e112.
10 Q. He, Z. Jiang, H. Jiang, S. Han, G. Yang, X. Yuan and H. Zhu, *Nanoscale*, 2024, **16**, 14310–14318.
11 S. Qian, Z. Wang, Z. Zuo, X. Wang, Q. Wang and X. Yuan, *Coord. Chem. Rev.*, 2022, **451**, 214268.
12 G. Yang, Z. Wang, F. Du, F. Jiang, X. Yuan and J. Y. Ying, *J. Am. Chem. Soc.*, 2023, **145**, 11879–11898.
13 M. M. Zhang, X. Y. Dong, Z. Y. Wang, H. Y. Li, S. J. Li, X. Zhao and S. Q. Zang, *Angew. Chem., Int. Ed.*, 2020, **59**, 10052–10058.
14 H. Xiang, Y. Wang, X. Xu, C. Ruan, K. Wang, W. Cheng, M. Zhou, X. Liu and C. Yao, *J. Am. Chem. Soc.*, 2024, **146**, 28572–28579.
15 X. Wang, B. Yin, L. Jiang, C. Yang, Y. Liu, G. Zou, S. Chen and M. Zhu, *Science*, 2023, **381**, 784–790.
16 M. A. Abbas, P. V. Kamat and J. H. Bang, *ACS Energy Lett.*, 2018, **3**, 840–854.

17 H. Zhang, H. Liu, Z. Tian, D. Lu, Y. Yu, S. Cestellos-Blanco, K. K. Sakimoto and P. Yang, *Nat. Nanotechnol.*, 2018, **13**, 900–905.

18 Y. Jin, Q.-C. Peng, S. Li, H.-F. Su, P. Luo, M. Yang, X. Zhang, K. Li, S.-Q. Zang, B. Z. Tang and T. C. W. Mak, *Natl. Sci. Rev.*, 2022, **9**, nwab216.

19 F. Liu, T. Yang, X. Chang, L. Chen, C. Cheng, X. Peng, H. Liu, Y. Zhang and X. Chen, *Natl. Sci. Rev.*, 2024, **11**, nwae113.

20 Y. Xiao, Z. Wu, Q. Yao and J. Xie, *Aggregate*, 2021, **2**, 114–132.

21 L. Shang, J. Xu and G. U. Nienhaus, *Nano Today*, 2019, **28**, 100767.

22 H. Wang, H. Xing, J. Gong, H. Zhang, J. Zhang, P. Wei, G. Yang, J. W. Y. Lam, R. Lu and B. Z. Tang, *Mater. Horiz.*, 2020, **7**, 1566–1572.

23 Z. Wu, Q. Yao, O. J. H. Chai, N. Ding, W. Xu, S. Zang and J. Xie, *Angew. Chem., Int. Ed.*, 2020, **59**, 9934–9939.

24 Z. Lu, Y. J. Yang, W. X. Ni, M. Li, Y. Zhao, Y. L. Huang, D. Luo, X. Wang, M. A. Omary and D. Li, *Chem. Sci.*, 2021, **12**, 702–708.

25 M. M. S. Lee, E. Y. Yu, J. H. C. Chau, J. W. Y. Lam, R. T. K. Kwok and B. Z. Tang, *Adv. Mater.*, 2024, 2407707.

26 C. J. L. Murray, K. S. Ikuta, F. Sharara and L. Swetschinski, *Lancet*, 2022, **399**, 629–655.

27 K. Zheng and J. Xie, *Acc. Mater. Res.*, 2021, **2**, 1104–1116.

28 M. Tang, J. Zhang, C. Yang, Y. Zheng and H. Jiang, *Front. Chem.*, 2020, **8**, 181.

29 S. Yougbare, T.-K. Chang, S.-H. Tan, J.-C. Kuo, P.-H. Hsu, C.-Y. Su and T.-R. Kuo, *Int. J. Mol. Sci.*, 2019, **20**, 2924.

30 Z. Pang, N. Ren, Y. Wu, J. Qi, F. Hu, Y. Guo, Y. Xie, D. Zhou and X. Jiang, *Adv. Mater.*, 2023, **35**, 2303562.

31 H. Zhu, S. Wang, Y. Wang, C. Song, Q. Yao, X. Yuan and J. Xie, *Biomaterials*, 2022, **288**, 121695.

32 Y. Zheng, W. Liu, Y. Chen, C. Li, H. Jiang and X. Wang, *J. Colloid Interface Sci.*, 2019, **546**, 1–10.

33 N. Liu, Y. Wang, Z. Wang, Q. He, Y. Liu, X. Dou, Z. Yin, Y. Li, H. Zhu and X. Yuan, *Nanoscale*, 2022, **14**, 8183–8191.

34 D. Hikosou, S. Saita, S. Miyata, H. Miyaji, T. Furuike, H. Tamura and H. Kawasaki, *J. Phys. Chem. C*, 2018, **122**, 12494–12501.

35 Z. Zhao and Y. Li, *Colloids Surf., B*, 2020, **195**, 111244.

36 W.-F. Lai, W.-T. Wong and A. L. Rogach, *Adv. Mater.*, 2020, **32**, 1906872.

37 Y. Wang, Z. Zuo, Z. Wang, Y. Wu, J. Linghu, Y. Liu, H. Zhu, X. Dou, T. Feng and X. Yuan, *Chem. Eng. J.*, 2024, **492**, 152216.

38 P. K. Khanna, S. Gaikwad, P. V. Adhyapak, N. Singh and R. Marimuthu, *Mater. Lett.*, 2007, **61**, 4711–4714.

39 H. Zhu, N. Goswami, Q. Yao, T. Chen, Y. Liu, Q. Xu, D. Chen, J. Lu and J. Xie, *J. Mater. Chem. A*, 2018, **6**, 1102–1108.

40 K. Li and Z. Xue, *Mater. Chem. Phys.*, 2014, **148**, 253–261.

41 W. Wei, Y. Lu, W. Chen and S. Chen, *J. Am. Chem. Soc.*, 2011, **133**, 2060–2063.

42 H. Miao, D. Zhong, Z. Zhou and X. Yang, *Nanoscale*, 2015, **7**, 19066–19072.